

A Bio-Inspired Active Radio-Frequency Silicon Cochlea

Soumyajit Mandal, *Student Member, IEEE*, Serhii M. Zhak, and Rahul Sarpeshkar, *Senior Member, IEEE*

Abstract—Fast wideband spectrum analysis is expensive in power and hardware resources. We show that the spectrum-analysis architecture used by the biological cochlea is extremely efficient: analysis time, power and hardware usage all scale linearly with N , the number of output frequency bins, versus $N \log(N)$ for the Fast Fourier Transform. We also demonstrate two on-chip radio frequency (RF) spectrum analyzers inspired by the cochlea. They use exponentially-tapered transmission lines or filter cascades to model cochlear operation: Inductors map to fluid mass, capacitors to membrane stiffness and active elements (transistors) to active outer hair cell feedback mechanisms. Our RF cochlea chips, implemented in a $0.13 \mu\text{m}$ CMOS process, are $3 \text{ mm} \times 1.5 \text{ mm}$ in size, have 50 exponentially-spaced output channels, have 70 dB of dynamic range, consume $< 300 \text{ mW}$ of power and analyze the radio spectrum from 600 MHz to 8 GHz. Our work, which delivers insight into the efficiency of analog computation in the ear, may be useful in the front ends of ultra-wideband radio systems for fast, power-efficient spectral decomposition and analysis. Our novel rational cochlear transfer functions with zeros also enable improved audio silicon cochlea designs with sharper rolloff slopes and lower group delay than prior all-pole versions.

Index Terms—Bio-inspired, cochlear models, radio frequency (RF), silicon cochlea, spectrum analysis.

I. INTRODUCTION

THE mammalian cochlea, or inner ear, is an amazing sensory instrument that transforms sound frequencies into spatially and temporally-varying excitation patterns of the auditory nerve. It performs this task over a wide range of input frequencies and amplitudes using very little power. In humans, the approximate values of these performance metrics are three decades, 120 dB, and $14 \mu\text{W}$, respectively [1]. The cochlea is a hydro-mechanical system; incoming sounds set up traveling waves on the basilar membrane (BM) and in the fluids that surround it [2], [3]. The properties of the BM scale approximately exponentially with position: The membrane gradually becomes wider and less stiff, and resonates at lower frequencies. Thus, high frequency sounds excite responses towards the beginning, or basal part, of the cochlea, while low frequency sounds excite responses towards the end, or apical part. In other words, the cochlea uses a *frequency-to-space transformation* to perform audio spectral analysis.

Manuscript received November 04, 2008; revised March 17, 2009. Current version published May 28, 2009. The work of S. Mandal was partially supported by a Poitras pre-doctoral fellowship.

The authors are with the Department of Electrical Engineering and Computer Science, Massachusetts Institute of Technology, Cambridge, MA 02139 USA (e-mail: rahuls@mit.edu).

Digital Object Identifier 10.1109/JSSC.2009.2020465

Active feedback, mediated by outer hair cells (OHCs) located on the BM, amplifies the amplitude of the cochlear traveling wave and improves frequency selectivity. OHCs have been the subject of much research [4]–[12]. The cochlea performs highly resource-efficient distributed computation by exploiting the properties of a physical medium. Distributed analog computation has been used to build several efficient engineering systems, both at radio frequencies (RF) [13]–[16] and at lower frequencies [17].

Electronic circuit models of cochlear mechanics, also known as silicon cochleas, have thus far only been integrated on-chip at audio [1], [18]–[21], though simulations of a frequency-shifted cochlear model operating between 300 kHz and 1 MHz were presented in [22]. The idea of an “RF cochlea” was first proposed in [23]. A few building-block circuits for this RF cochlea were described in [24]. Some completely passive electronic cochleas that operate at RF using discrete components or multi-chip modules have also recently been reported [25]–[27].

In this paper we demonstrate the first integrated-circuit implementation of the cochlear spectrum analysis algorithm using active electronic circuits operating at typical radio frequencies. We use a mechanical-to-electrical mapping to transform pressure P into voltage V , and volume velocity U into current I , respectively. Membrane stiffness is replaced by capacitance, fluid mass by inductance and active feedback mechanisms by circuits that create negative resistances. In this way, we mimic the mechanics of the biological cochlea, but at frequencies that are six orders of magnitude higher. A key advantage of operating at RF (as opposed to audio) is the availability of passive inductors, which have significantly lower noise and higher dynamic range than active inductors operating with the same power consumption [24].

This paper is organized as follows. Section II describes the spectrum analysis algorithm used by the biological cochlea, and analyzes reasons for its efficiency. Section III discusses novel bidirectional and unidirectional cochlear models that efficiently represent properties of the biological traveling wave architecture. Our unidirectional model is also useful for audio silicon cochlea designs. Section IV discusses circuit design of the RF cochlea. Section V discusses experimental results, while Section VI concludes the paper.

II. COCHLEAR SPECTRUM ANALYSIS

Fig. 1 graphically illustrates three common types of spectrum analyzers, including the cochlea. To first order, the cochlea can be modeled as a transmission line, shown in Fig. 2 where shunt admittances Y model sections of the BM, while the series impedances Z are inductors modeling fluid coupling. The values of Y and Z per unit length increase exponentially with position

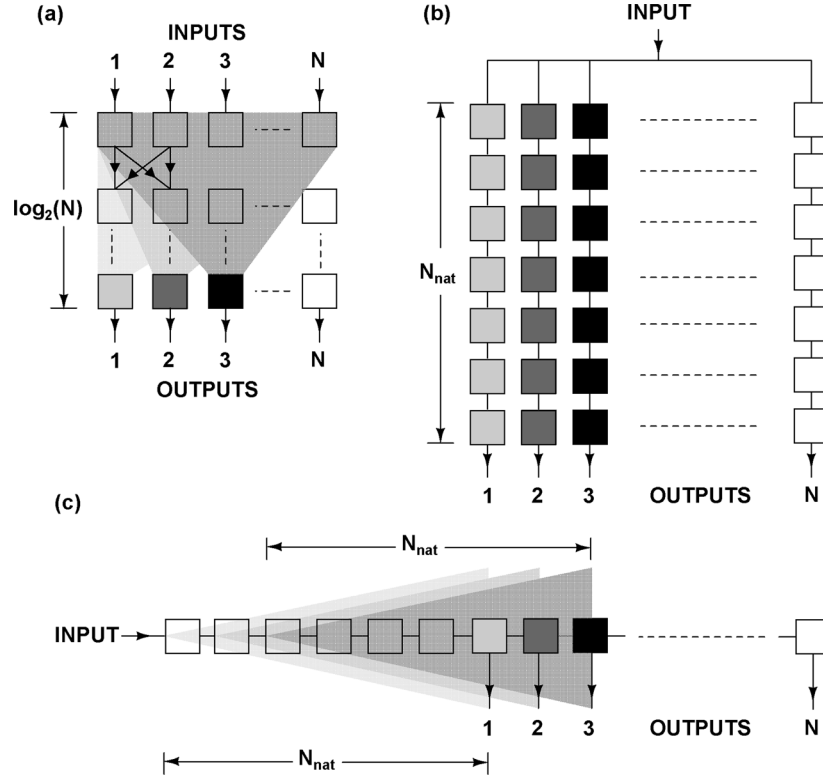


Fig. 1. Comparison of the spectral analysis algorithms of (a) the FFT, (b) a parallel bank of independent filters and (c) the cochlea. Blocks represent two-input multiply-and-add units in the FFT, elementary filters in the filter bank and cochlear stages in the cochlea. The ‘triangular’ sliding windows in the cochlea illustrate that cochlear transfer functions are created by contributions from approximately N_{nat} filters basal to that output. Therefore, only one new stage needs to be added to create each new output.

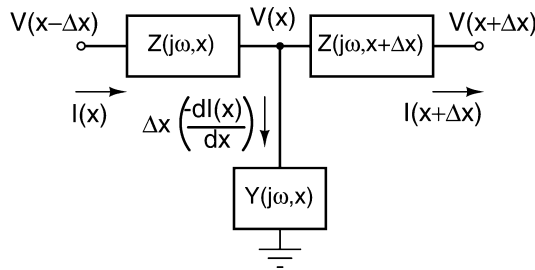


Fig. 2. A generic spatially-varying one-dimensional transmission line, with series impedances represented by Z and shunt admittances by Y .

x [23], [28], i.e., $\propto \exp(x/l)$, where l is a constant that characterizes the length scale on which cochlear properties vary from the basal ($x = 0$) to the apical end [28]. The transfer function $TF(x, \omega)$ of the cochlea is defined as the normalized current that flows through $Y(x)$ in response to an input tone with frequency ω [28]. It models the velocity of the BM. At a given position, the magnitude of the TF slowly increases with frequency, reaches its maximum value near a frequency $\omega_c(x) = \omega_c(0) \exp(-x/l)$, known as the center frequency, and then rapidly decreases.

In order to model the continuous cochlear transmission line with a finite number of components we spatially discretize it by lumping sections of line Δx long into individual stages. We assume Δx is constant; as a result the stages have exponentially-

spaced center frequencies. The number of stages per e-fold in center frequency is given by

$$N_{nat} = \frac{l}{\Delta x}. \quad (1)$$

The exponentially-tapered structure of the cochlea ensures that the TF at any position is produced by a “sliding window” of the approximately N_{nat} stages basal of that position, as shown in Fig. 1. The magnitude of each TF peaks around its center frequency ω_c , and thus selects a frequency “bin” centered about ω_c . Any cochlear TF is well approximated as a cascade of N_{nat} identical stages, which gives cochlear TFs a very sharp rolloff slope [1]. The frequency resolution of the cochlea is ultimately set by the sharpness of these high-frequency roll-off slopes, which for a given signal-to-noise ratio, sets the minimum frequency ratio that can be discriminated by adjacent cochlear stages.

The analysis time τ_i of a spectrum analyzer is defined as the time taken to resolve the i -th frequency bin. In the cochlea, the analysis time is equal to the sum of the settling times of stages basal of i , which is approximately equal to $N_{nat}/\omega_c(i)$. Therefore, the analysis time for the whole spectrum is on the order of N_{nat} cycles of the lowest analyzed frequency. In addition, the total number of stages is given by $N = N_{nat}(\ln(\beta) + 1)$, where β is the ratio of maximum and minimum analyzed frequencies, and the ‘1’ accounts for the fact that the very first cochlear output needs an extra N_{nat} stages basal to it. Thus, for a

given value of β , we get $N \propto N_{\text{nat}}$, which implies that $\tau_i \propto N$. In order to make the shape of TF independent of i we implement cochlear stages as frequency-scaled versions of a common prototype [18]. As a result, the hardware and power requirements of the cochlea also scale as the total number of filters, i.e., N .

A parallel bank of constant- Q , independent filters can also be used to decompose a signal into exponentially-spaced frequency bins. In order to get frequency resolution similar to the cochlea each independent filter must have order $2N_{\text{nat}}$. Such filters can be formed by cascading N_{nat} second-order filter stages, as shown in Fig. 1. There are N such filters, which, unlike in the cochlea, are not shared between outputs. Thus, the hardware cost, as measured by the total number of second-order filter stages, scales like $N \times N_{\text{nat}} \propto N^2$ if β is fixed. However, the time taken for spectrum analysis in the filter bank is given by the sum of the settling times of the N_{nat} sections in each filter, which scales like N .

The output bins of both the cochlea and parallel filter banks are available and updated in parallel, which allows them to continuously monitor the whole spectrum. This behavior is in contrast to most commercial RF spectrum analyzers, which are of the swept-sine or super-heterodyne type. In this type of analyzer a single frequency bin is sampled and updated at a given time, causing aliasing of non-stationary spectra. The sampling rate scales as $1/N^2$, i.e., the time to analyze the whole spectrum scales as N^2 [29]. However, the hardware requirements for this type of analyzer are independent of N , i.e., $O(1)$.

The Fast Fourier Transform (FFT) uses constant-bandwidth frequency bins, unlike the cochlea and constant- Q parallel filter banks. It takes $O(N \ln(N))$ time (measured by the number of multiply-and-add operations) and uses $O(N \ln(N))$ hardware (measured by the number of multipliers and adders) to perform spectrum analysis.

Thus, it appears that the cochlear spectral analysis algorithm delivers the most efficient trade-off between analysis time and hardware cost. It exploits the scale-invariant nature of an exponential to achieve $O(N)$ scaling in both quantities.

III. SYSTEM DESIGN

A. Bidirectional Cochlear Model

The equations for voltage V (corresponding to fluid pressure P) and current I (corresponding to volume velocity U) on the spatially-varying transmission line shown in Fig. 2 in sinusoidal steady-state are given by

$$\frac{dV}{dx} = -Z(\omega, x)I \quad \frac{dI}{dx} = -Y(\omega, x)V \quad (2)$$

where $Z(\omega, x)$ and $Y(\omega, x)$ are the impedance and admittance per unit length of the line. We now define $s_n = j\omega/\omega_c(x)$ as a dimensionless frequency variable that is normalized by the center frequency $\omega_c(x) = \omega_c(0) \exp(-x/l)$ at the position of interest. Because of the exponential scaling in the cochlea, we have $Z(\omega \exp(-x/l), x) = Z(\omega, 0)$ and $Y(\omega \exp(-x/l), x) = Y(\omega, 0)$, i.e., the impedances and admittances at any two positions in the cochlea are identical if we exponentially scale the frequencies at which they are compared.

Since $ds_n/dx = s_n/l$, we can eliminate the separate dependencies on ω and x by rewriting (2) as

$$\begin{aligned} \frac{dV}{ds_n} &= \frac{dV}{dx} \times \frac{dx}{ds_n} = - \left(\frac{lZ(s_n)}{s_n} \right) I \\ \frac{dI}{ds_n} &= \frac{dI}{dx} \times \frac{dx}{ds_n} = - \left(\frac{lY(s_n)}{s_n} \right) V \end{aligned} \quad (3)$$

Hereafter, we use the convention that Z and Y refer to impedance and admittance per unit length in the continuous transmission line, Z_d and Y_d refer to impedances and admittances in the spatially-discretized, or lumped transmission line, and Z_n and Y_n are normalized, dimensionless forms of Z_d and Y_d . Each stage contains a series impedance Z_d and a shunt admittance Y_d , given by

$$Z_d = (\Delta x)Z(s_n) \quad Y_d = (\Delta x)Y(s_n) \quad (4)$$

The series impedance Z_d consists of an inductance that models fluid mass and increases exponentially with position, resulting in

$$\begin{aligned} Z_d(s_n) &= j\omega L_0 \exp(x/l) \\ &= \frac{\omega}{\omega_c(x)} (\omega_c(0) \exp(-x/l) \times L_0 \exp(x/l)) \\ &= s_n \omega_c(0) L_0 \end{aligned} \quad (5)$$

where $L_0 = (\Delta x)L(0)$, and $L(0)$ is the inductance per unit length at $x = 0$. The normalized, dimensionless forms of Z_d and Y_d are given by

$$Z_n = \frac{Z_d}{Z_0} \quad Y_n = Y_d Z_0 \quad (6)$$

The normalizing impedance Z_0 is a constant that, in a real implementation, scales all dimensionless impedances and provides a degree of freedom in the design. In the RF cochlea, Z_0 is chosen to make on-chip implementation practical, as we discuss later. From (5) and (6), Z_n is given by

$$Z_n(s_n) = s_n \left(\frac{\omega_c(0)L_0}{Z_0} \right) = s_n Q_{\text{line}} \quad (7)$$

where $Q_{\text{line}} \equiv \omega_c(0)L_0/Z_0$ is a dimensionless constant. The normalized shunt admittance Y_n models the complex behavior of the organ of Corti. In an important paper [28], Zweig used experimental measurements to propose the following form for Y_n :

$$Y_n(s_n) = \frac{s_n}{s_n^2 + \delta s_n + 1 + \rho \exp(-\psi s_n)} \quad (8)$$

where δ, ρ and ψ are constants. Zweig's admittance function can be interpreted as a feedback loop containing an RLC resonator and a pure delay. Its frequency response is shown in Fig. 3 for the following parameter values (obtained from [28]): $\delta = -0.122, \rho = 0.142, \psi = 2\pi \times 1.74$. Unfortunately, the function cannot be synthesized with a finite number of lumped circuit elements because it is not rational. We therefore used

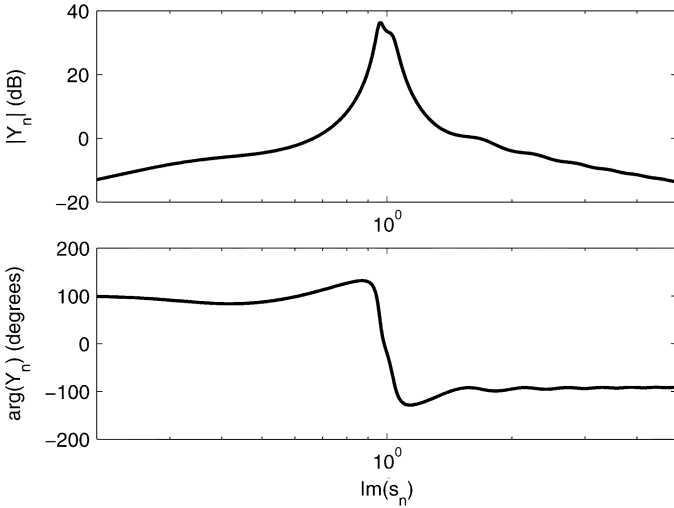


Fig. 3. Normalized BM admittance Y_n proposed by Zweig [28].

a rational function to approximate (8), [30]. The function we chose is given by

$$Y_n(s_n) = \frac{s_n \left(s_n^2 + \frac{\mu}{Q} s_n + \mu^2 \right)}{\mu^2 (s_n^2 + 2ds_n + 1)^2} \quad (9)$$

where μ , Q and d are constants. This admittance is the simplest rational function that contains all essential features of (8). These features are: two pairs of high- Q complex poles, a pair of zeros, capacitive behavior at low frequencies, and inductive behavior at high frequencies. Allowable values of μ , Q and d at all amplitudes are constrained by the requirement that zero-crossings in the transient response remain approximately invariant with input amplitude, like in the biological cochlea [10]. We used the following parameter values in our bidirectional cochlea design: $d = 0.1$, $\mu = 0.76$ and $Q = 3.8$. The resultant form of Y_n , which is shown in Fig. 4(a) and (b), is quite similar to Zweig's function, which is shown in Fig. 3.

At frequencies much smaller than the maximum operating frequency $\omega_c(0)$ the input impedance of the cochlea is given by the following standard expression for a continuous transmission line with series impedances Z_d and shunt admittances Y_d :

$$Z_{\text{in}} \approx \sqrt{Z_d/Y_d} = Z_0 \sqrt{Z_n/Y_n}. \quad (10)$$

When $s_n \ll 1$, we see from (9) that $Y_n \approx s_n$. Therefore, at frequencies that are much smaller than the local center frequency Y_n looks like a capacitor. Substituting for Y_n and Z_n in (10), we find that the input impedance at frequencies much smaller than $\omega_c(0)$ is given by

$$Z_{\text{in}} = \sqrt{\omega_c(0)L_0Z_0} = Z_0\sqrt{Q_{\text{line}}}. \quad (11)$$

We usually fix $Z_{\text{in}} = 50 \Omega$ for compatibility with standard RF test equipment. The sizes of capacitors in the design scale like

$$C_0 = \frac{1}{\omega_c(0)Z_0}. \quad (12)$$

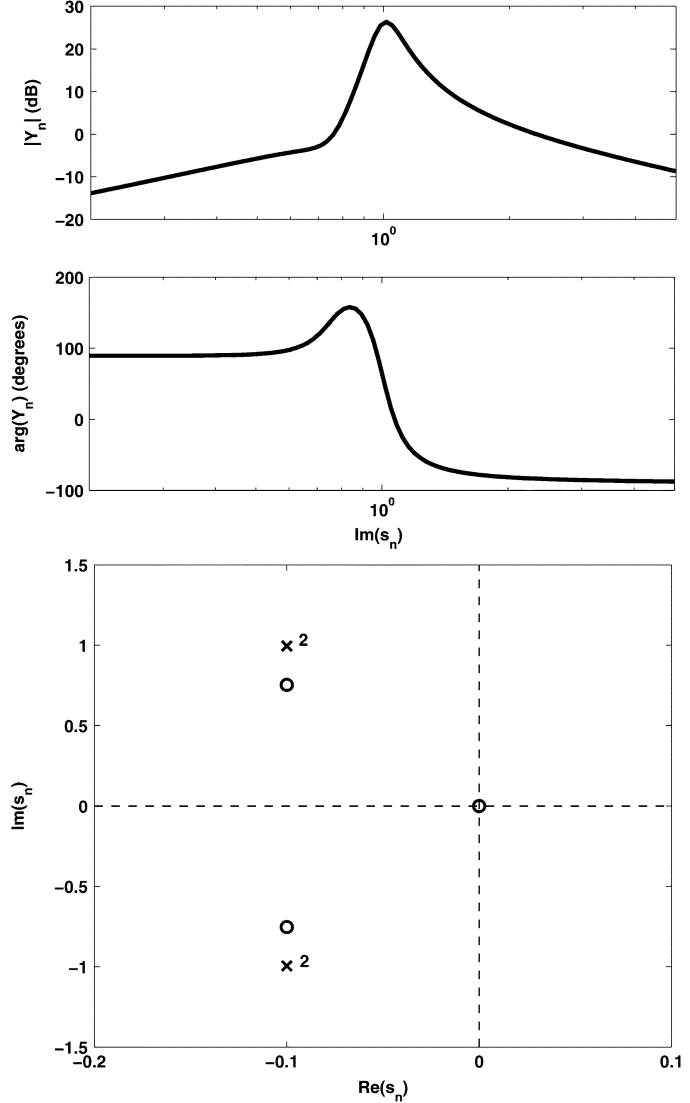


Fig. 4. (a) Normalized BM admittance Y_n used in the cochlea. (b) Pole-zero plot for Y_n .

Equivalently, we have $Z_{\text{in}} = \sqrt{L_0/C_0}$. The exponential decrease of center frequency with position is accomplished by increasing inductor and capacitor values in Z_d and Y_d exponentially with stage number i , i.e., making L_i and C_i (and all other inductors and capacitors used to implement Y_d) scale as $\exp(i/N_{\text{nat}})$, while resistances remain fixed [31], [32].

The system of first-order ODEs shown in (3) can be combined into a single second-order ODE, given by

$$\frac{d^2V}{ds_n^2} = k_n^2(s_n)V \quad (13)$$

where $k_n = l\sqrt{ZY}/s_n = N_{\text{nat}}\sqrt{Z_nY_n}/s_n$ is a dimensionless variable. If k_n was constant with s_n , as in a uniform transmission line, the solution to (13) would simply be the complex exponential $\exp(k_n s_n)$. Now assume that k_n is not constant, but, as in the cochlea, varies slowly with s_n , i.e., such that $|dk_n/ds_n| \ll k_n$. In this case, we can use the well known

Wentzel-Kramers-Brillouin (WKB) approximation to solve (13), [28]. The result is

$$V(s_n) = \frac{\alpha}{\sqrt{k_n(s_n)}} \exp\left(\pm \int_0^{s_n} k_n(s') ds'\right) \quad (14)$$

where α is a constant. The *transfer function* (TF) of the cochlea, which is defined as the current flowing through the shunt admittance Y , normalized by the input current $I(0)$ [28], can be written as

$$\begin{aligned} \text{TF}(s_n) &= \frac{\Delta x}{I(0)} \frac{dI}{dx} = \frac{\Delta x}{I(0)} \frac{dI}{ds_n} \times \frac{ds_n}{dx} \\ &= \frac{\Delta x}{l} \frac{s_n}{I(0)} \frac{dI}{ds_n}. \end{aligned} \quad (15)$$

Substituting dI/ds_n from (3) in (15), and remembering that $N_{\text{nat}} = l/(\Delta x)$, we find that

$$\text{TF}(s_n) = \frac{s_n}{Z_0 Q_{\text{line}}} \left(\frac{k_n}{N_{\text{nat}}}\right)^2 \frac{V(s_n)}{I(0)}. \quad (16)$$

We can substitute $V(s_n)$ from (14) into the expression for the cochlear TF defined in (16), to find that the cochlear TF is proportional to

$$\text{TF}(s_n) \propto s_n k_n^{3/2} \left[c_1 \exp\left(+ \int_0^{s_n} k_n ds'\right) + c_2 \exp\left(- \int_0^{s_n} k_n ds'\right) \right] \quad (17)$$

where c_1 and c_2 are constants determined by $I(0)$, N_{nat} , Z_0 and boundary conditions. The two terms correspond to wave propagation in the $+x$ (forward) and $-x$ (reflected) directions. The reflected wave is undesirable, and its amplitude should be minimized.

The center frequency of the last, or apical, cochlear stage is given by $\omega_{c,\text{min}} = \omega_c(0) \exp(-N/N_{\text{nat}})$, where N is the total number of stages. In order to reduce reflections from the apex the transmission line must be terminated with an impedance-matched load. We found that a termination impedance consisting of a resistor R_t in series with an inductor L_t provides adequate matching over the frequency range of interest, namely $0 < \omega < \omega_{c,\text{min}}$. We use $R_t = Z_{\text{in}}$, which provides a match at frequencies much smaller than $\omega_{c,\text{min}}$. We also make the magnitude of L_t 's impedance at $\omega_{c,\text{min}}$ equal to Z_{in} , which provides a match at frequencies comparable to $\omega_{c,\text{min}}$. Thus, L_t is given by

$$L_t = \frac{Z_{\text{in}}}{\omega_{c,\text{min}}} = \frac{Z_{\text{in}} \exp(N/N_{\text{nat}})}{\omega_c(0)}. \quad (18)$$

In order for our lumped transmission line to closely approximate the original continuous line each stage should only change the phase of TF, i.e., $\int_0^{s_n} k_n ds'$, by a small amount. If this condition is not met the spatial discretization becomes too coarse, resulting in unwanted inter-stage reflections that show up as sec-

ondary peaks in the cochlear TF. In order to avoid such reflections, we should have

$$\begin{aligned} |\Delta s_n \times k_n| &\ll 1 \\ \Rightarrow \left| \left(\frac{ds_n}{dx} \right) \Delta x \times k_n \right| &\ll 1 \\ \Rightarrow \frac{|s_n k_n|}{N_{\text{nat}}} &\ll 1 \end{aligned} \quad (19)$$

where Δs_n is the change in s_n due to a single stage, and we have used the fact that $ds_n/dx = s_n/l$. Thus, inter-stage reflections increase as $|s_n| = \omega/\omega_c(x)$, the ratio of the input frequency to the best frequency at that location, increases. In other words, a fixed-frequency input tone will suffer increasing reflections as it propagates, since $\omega_c(x)$ decreases exponentially with increasing x .

For a given value of s_n , inter-stage reflections can be reduced by reducing $|k_n|$ and increasing N_{nat} . However, signal gain, i.e., $|\text{TF}|$, increases with $|k_n|$, as may be seen from (17). On the other hand increasing N_{nat} is undesirable because of increased chip area, power consumption, and output noise. The designer must compromise between these conflicting performance requirements.

By substituting $k_n = N_{\text{nat}} \sqrt{Z_n Y_n} / s_n$ and using the known values of Z_n and Y_n , the no-reflection condition in (19) can be rewritten as

$$\sqrt{Q_{\text{line}}} \left| \frac{s_n \sqrt{s_n^2 + \mu s_n / Q + \mu^2}}{\mu (s_n^2 + 2ds_n + 1)} \right| \ll 1. \quad (20)$$

Since the values of μ , Q and d are fixed, we must reduce Q_{line} to reduce inter-stage reflections. The quantity Q_{line} has a simple physical interpretation: it is the ratio of the amount of reactive energy stored within each stage, which is given by $L_0 I^2 / 2$, to the energy transferred per cycle (i.e., in a time $1/\omega_c(0)$) to the other stages. The latter quantity is given by $Z_0 I^2 / (2\omega_c(0))$, where I is the current along the line. Using (12), we can also rewrite Q_{line} in the suggestive form

$$Q_{\text{line}} = \frac{2\omega_c(0)}{\omega_{\text{cutoff}}(0)}. \quad (21)$$

Here $\omega_{\text{cutoff}}(0) = 2/\sqrt{L_0 C_0}$ is the cutoff frequency of the lumped transmission line. Wave propagation on lumped lines is only possible at frequencies less than the cutoff frequency.

B. Unidirectional Cochlear Model

In the biological cochlea, backward wave propagation is relatively unimportant except for the production of otoacoustic emissions [11]. If we ignore such waves, the bidirectional transmission line can be simplified into a cascade of unidirectional filters. We refer to this architecture as the *unidirectional RF cochlea*.

The transfer functions $H(s_n)$ for filters in the unidirectional cochlea can be derived from a WKB-type solution of the wave equation by making a series of further approximations [24], [30]. The essence of cochlear operation is collective amplification, as exemplified by the exponential part of the transfer function shown in (17). For simplicity, therefore, we ignore the pre-

exponential terms. The reflected wave is also neglected, making the structure unidirectional. The exponential term is modeled by breaking up the integral, which extends from 0 to s_n , into small parts extending from s_{i-1} to s_i , where i is an integer:

$$\begin{aligned} \exp\left(-\int_0^{s_n} k_n ds'\right) &= \prod_i \exp\left(-\int_{s_{i-1}}^{s_i} k_n ds'\right) \\ &\equiv \prod_i H_i. \end{aligned} \quad (22)$$

We note that the expression above looks like the transfer function of a cascade of unidirectional filters with transfer functions H_i . We assume that each filter models the action of a piece of transmission line Δx long. Thus, the i th filter models the piece of line between $x = (i-1)\Delta x$ and $x = i\Delta x$. By using the definition of s_n , we have

$$s_i = \frac{j\omega}{\omega_c(0) \exp(-i\Delta x/l)} = s_0 \exp(i/N_{\text{nat}}) \quad (23)$$

where $s_0 = j\omega/\omega_c(0)$. Thus, the values of s_i increase exponentially, i.e., proportional to $\exp(i/N_{\text{nat}})$. In other words, we have N_{nat} filters per e-fold in frequency. Now define $\Delta s_i = s_i - s_{i-1}$. If N_{nat} is large enough, we may assume that k_n remains approximately constant between s_i and s_{i-1} . Therefore, the integral that defines H_i can be simplified to

$$H_i \approx \exp(-\Delta s_i \times k_n). \quad (24)$$

If $N_{\text{nat}} \gg 1$, $|\Delta s_i \times k_n| \ll 1$ and each transfer function can be approximated by using the identity $\exp(-x) \approx 1/(1+x)$ since $|x| \ll 1$. Also, we may write $\Delta s_i \approx (\Delta x)(ds_n/dx) = s_i/N_{\text{nat}}$. Therefore, H_i is given by

$$H_i \approx \frac{1}{1 + \frac{s_i k_n(s_i)}{N_{\text{nat}}}}. \quad (25)$$

We see that each transfer function is only a function of s_i , which scales exponentially along the cascade, and N_{nat} , which is constant, but can differ from its value in the bidirectional cochlea. Therefore, the transfer functions are simply frequency-scaled versions of each other and we can represent all of them using the single normalized frequency variable s_n . By substituting in $k_n = N_{\text{nat}} \sqrt{Z_n Y_n}/s_n$, we get the following normalized transfer function:

$$H_n(s_n) = \frac{1}{1 + \sqrt{Z_n Y_n}}. \quad (26)$$

In order to make $H_n(s_n)$ rational, we choose $Q = 0.5$ in (9). This choice makes $Z_n Y_n$ a perfect square, and $H_n(s_n)$ is given by

$$H_n(s_n) = \frac{s_n^2 + 2ds_n + 1}{(1 + \sqrt{Q_{\text{line}}/\mu})s_n^2 + (2d + \sqrt{Q_{\text{line}}})s_n + 1} \quad (27)$$

where $Q_{\text{line}} = \omega_c(0)L_0/Z_0$, as in the bidirectional cochlea. We used the following parameter values in our unidirectional cochlea design: $d = 0.1$, $\mu = 0.3$ and $Q_{\text{line}} = 0.5$ [24]. Our filter TF is shown in Fig. 5(a) and (b). Since it contains a pair of poles and a pair of complex zeros, it differs from the

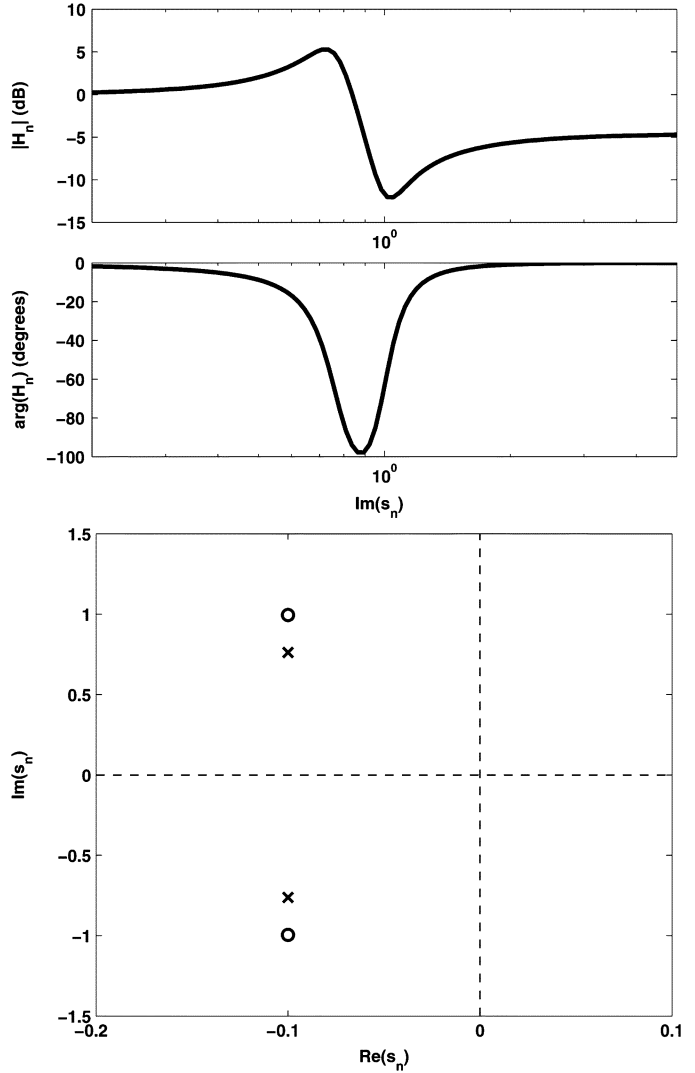


Fig. 5. (a) Normalized TF H_n used in the unidirectional cochlea. (b) Pole-zero plot for H_n .

all-pole TF's previously used to build audio-frequency silicon cochleas [1], [18]. In addition to reducing group delay, the figure shows that the zeros also result in an asymmetric frequency response close to the peak of the TF, with a sharper drop-off on the high-frequency side that increases the frequency resolution of the cochlear TFs. The filter transfer function actually implemented on-chip included an additional high-frequency zero and two additional high-frequency poles because they made the circuit significantly easier to design. These additional poles and zeros do not have a significant effect on the cochlear transfer function.

IV. CIRCUIT DESIGN

A. Bidirectional Cochlea

Equation (9) shows that the BM admittance Y must tend to zero as $s_n \rightarrow \infty$. However, integrated circuits contain parasitic capacitances that, at high frequencies, become large admittances in parallel with Y . A more robust design is obtained by reversing the mapping between mechanical and electrical domains, i.e., representing pressure P by current I , and volume

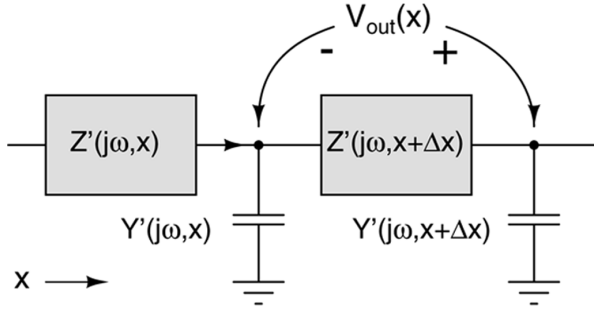


Fig. 6. The impedance-transformed cochlear model that was implemented on-chip.

velocity U by voltage V . This new mapping transforms impedances to admittances and vice versa, so we get the transmission line structure shown in Fig. 6, where $Z'_n = Y_n Q_{\text{line}}$ and $Y'_n = Z_n / Q_{\text{line}}$. The output variable changes from the shunt current dI/dx to the voltage across the series impedances, i.e., $V_{\text{out}} \equiv (\Delta x) \times (dV/dx)/V(0)$. Note that parasitic shunt capacitances can now be absorbed into the line. Another advantage of this design is that the output, being the difference in voltage between two nodes, is resistant to unwanted common-mode signals on the ground node. The wave number is unchanged and the cochlear TFs have the same frequency dependence as before. However, impedances and admittances are interchanged, so the series $R-L$ termination network becomes a parallel $R-C$ network. We used the following parameter values in our bidirectional cochlea implementation: $\omega_c(0) = 2\pi \times 10 \times 10^9$ rad/s, $C(0) = 70$ fF, $N_{\text{nat}} = 20$, $Z_0 = 225 \Omega$, $Q_{\text{line}} = 0.05$ and $Z_{\text{in}} = 50 \Omega$.

For the realistic parameter values used to draw Fig. 4(a), the series impedance Z'_n is not physically realizable using only passive elements. In fact, it needs at least two resistances, one of which, say R_1 , must be negative to pump energy into the traveling wave in regions basal of the peak and increase gain. The second resistance R_2 must be positive for overall stability. A simplified version of our stage design is shown in Fig. 7. Each Z'_n consists of two resonators that are coupled both inductively and capacitively.

At positions far before the peak the negative resistance R_1 cannot pump energy into the traveling wave, since Z'_n is dominated by the inductor L_2 . Any parasitic series resistance in L_2 now absorbs energy from the wave, causing it to attenuate. An additional negative resistance, R_{LL} in parallel with the shunt admittance C_3 is used to cancel such attenuation.

A more complete circuit diagram of our implementation of a single bidirectional cochlea stage is shown in Fig. 8. The DC voltage on the line (i.e., the DC value of V_1 and V_2 for every stage) is determined by a low-frequency negative feedback loop that sets V_P to an appropriate value. The loop, which runs continuously, uses an integrator to sense the DC line voltage and sets it equal to a reference voltage, normally $V_{DD}/2$. It does not interfere with normal cochlear operation because it has very low bandwidth.

A cross-coupled pair of nMOS transistors, M_1 and M_2 , creates the negative resistance R_1 . The bias current I_B through

the pair is set by the control voltage V_B . The impedance produced by the cross-coupled pair between V_1 and V_2 consists of a resistance $R_1 = -2/g_m$ in parallel with a capacitance $C_{\text{par}} = C_{gs}/2 + 2C_{gd}$, where g_m , the small signal transconductance, is an increasing function of I_B , and C_{gs} and C_{gd} are the gate-source and gate-drain capacitances, respectively. An important advantage of this topology is that C_{par} can be absorbed into C_1 .

The low-frequency line loss cancellation network is a single-ended negative resistor R_{LL} that is created in two stages. The voltage at V_2 is first amplified by a common-source amplifier. The output of this amplifier controls a current source, M_4 , that can sink or source current from V_2 . Because of the sign inversion produced by the amplifier, M_4 pushes current into the node when the voltage on it rises (and vice-versa) thereby creating a negative resistance of value $-1/(g_{m3}^2 R_B)$, where g_{m3} is the transconductance of M_3 and M_4 (assumed equal). The value of g_{m3} , and thus R_{LL} , is set by the bias voltage V_{B2} . The value of C_B is made large enough for the pole frequency g_{m3}/C_B to be much smaller than the center frequency at the location of interest, allowing the amplifier to reject the DC value of V_2 and only respond to RF (i.e., have a highpass characteristic). Without this loss-cancellation network, low frequencies would be attenuated by a factor $\alpha = 1 - R_{s2}/(R_{s2} + Z_{\text{in}})$ at every stage, where R_{s2} is the parasitic series resistance of L_2 (not drawn). With $Z_{\text{in}} = 50 \Omega$ by design and a typical $R_{s2} = 5 \Omega$, signals that peak at the end of the cochlea (after 50 stages) would be attenuated by a factor of about $\alpha^{50} \approx 10^{-2}$ (-40 dB) before reaching the apex.

The output voltages $V_{\text{out}}(n)$ are pre-amplified before their envelopes are detected and read out. Each pre-amplifier is a two stage, resistively-loaded, common source differential amplifier, with shunt-peaking in the early stages to increase the bandwidth and a voltage gain of approximately $A_{\text{pre}} = 16$ dB. Each envelope detector (ED) uses a diode-connected transistor for rectification and has a dead zone, for small signals, that is approximately equal to ϕ_T/κ , the linear range of the transistor. Here ϕ_T is the thermal voltage and κ is the sub-threshold constant. The preamplifiers reduce the input-referred dead-zone by a factor of A_{pre} , resulting in a detection threshold of $\phi_T/(\kappa A_{\text{pre}}) \approx 5.5$ mV_{pp}.

B. Unidirectional Cochlea

A simplified circuit diagram of our implementation of a single unidirectional cochlea filter is shown on the left-hand side of Fig. 9. Each filter, like in the bidirectional version, consists of two resonators that are coupled both inductively and capacitively. The transistor provides active gain and buffering. This topology is efficient because it uses a single transistor while also allowing parasitic capacitances associated with L_1 and L_2 to be absorbed into C_1 , C_2 and C_C .

A more detailed schematic of the filter is shown on the right-hand side of Fig. 9. The first important change from the simplified circuit shown on the left is that the resistor R_1 has been realized with an active element. The resistance seen looking into the source of the cascode transistor M_1 is given by $1/g_{m1}$, where

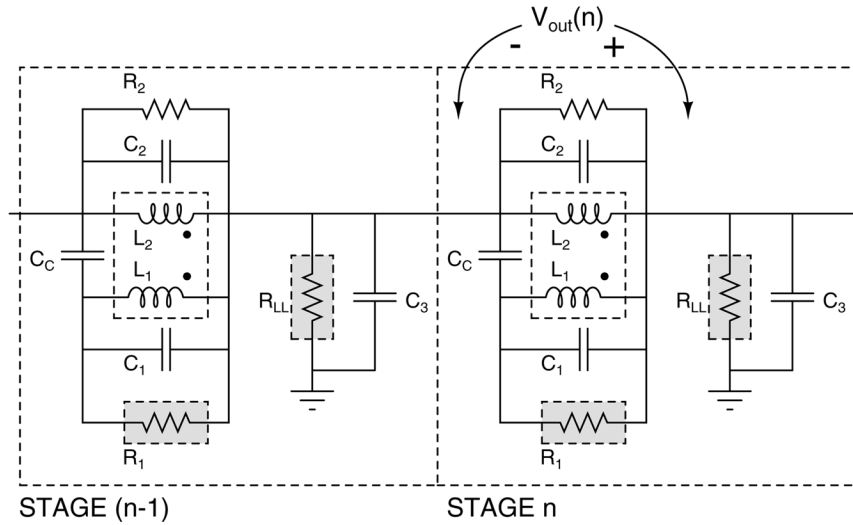


Fig. 7. Simplified bidirectional cochlea circuit diagram.

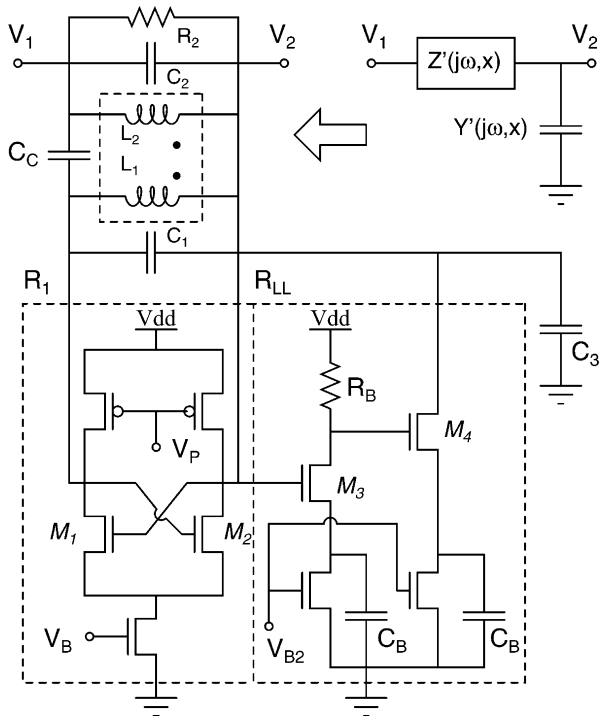


Fig. 8. A more detailed circuit diagram of a single bidirectional cochlea stage.

g_{m1} is the small-signal transconductance of M_1 . To this resistance we must add R_{s1} , the parasitic series resistance of L_1 , i.e., we have $R_1 = R_{s1} + 1/g_{m1}$. By implementing R_1 with a transistor we isolate L_1 from the power supply, eliminating the effect of parasitic inductances present there. The high-pass filter formed by C_3 and R_3 is designed to decouple the DC operating points of individual stages but act as a short at RF. At “low” frequencies (lower than the center frequency of the stage, but higher than the cut-in frequency of C_3 and R_3), the voltage gain of the filter is given by

$$\begin{aligned}
 TF(\omega_n \ll 1) &= (R_{s1} + 1/g_{m1}) \frac{g_{m2}}{g_{m2}R_{s2} + 1} \\
 &= \frac{g_{m2}}{g_{m1}} \left(\frac{1 + g_{m1}R_{s1}}{1 + g_{m2}R_{s2}} \right). \quad (28)
 \end{aligned}$$

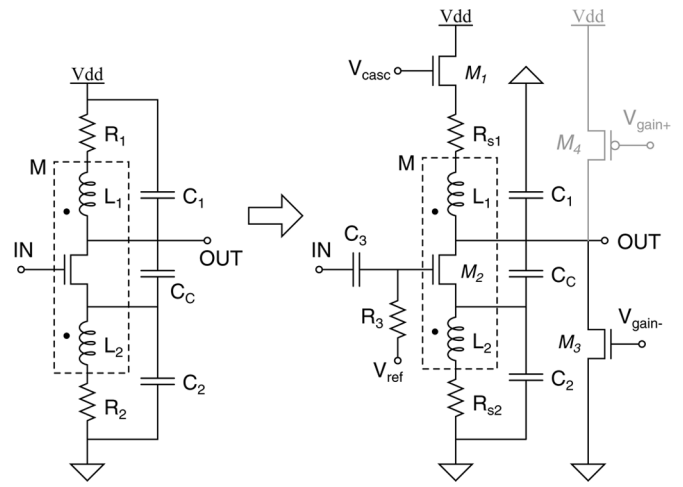


Fig. 9. A circuit diagram of a single unidirectional cochlea filter: simplified version on the left, more detailed implementation on the right. The transistor M_4 was not actually implemented on the current chip (see the text for an explanation).

Here $\omega_n = \text{Im}(s_n)$, g_{m2} is the transconductance of M_2 and R_{s2} is the parasitic series resistance of L_2 . In order to prevent low-frequency signals from either attenuating or blowing up as they propagate down the cascade we need $TF(\omega_n \ll 1)$ to be as close to 1 as possible. Assume for now that M_3 carries no bias current. In that case $g_{m1} \approx g_{m2}$, because M_1 and M_2 share the same bias current and were designed to have the same geometry. Also, R_{s1} and R_{s2} are parasitic components that are much smaller than $1/g_{m1}$ and $1/g_{m2}$, so $g_{m1}R_{s1} \ll 1$ and $g_{m2}R_{s2} \ll 1$. As a result, $TF(\omega_n \ll 1) \approx g_{m2}/g_{m1} = 1$, as required.

However, the equation above is only approximate. Since the inductor L_1 is in series with a large resistance, i.e., $1/g_{m1}$, it does not need to have a high quality factor. Therefore, we designed L_1 to have higher series resistance than L_2 in order to save layout area, i.e., $R_{s1} > R_{s2}$. Therefore, $g_{m1}R_{s1} > g_{m2}R_{s2}$, and we get a value of $TF(\omega_n \ll 1)$ that is somewhat > 1 .

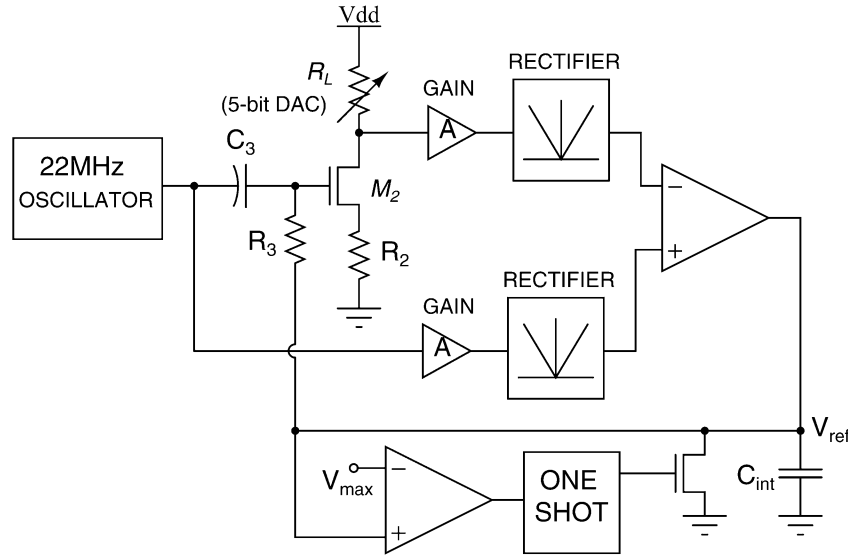


Fig. 10. Feedback loop used to set the bias voltage V_{ref} .

The voltage V_{gain-} sets the current through the transistor M_3 . By increasing V_{gain-} , we can make M_1 carry more current than M_2 , thus making $g_{m1} > g_{m2}$ and lowering $TF(\omega_n \ll 1)$. In order to set this low-frequency gain exactly equal to 1 we used a feedback loop. An on-chip oscillator running at 22 MHz continually injects a small calibration tone into the cascade. This signal does not interfere significantly with normal cochlear operation since its frequency is much lower than the lowest analysis frequency (600 MHz). The feedback loop uses an integrator to adjust the voltage V_{gain-} until the amplitudes of the calibration signal at the beginning and end of the cascade are equal to each other, thus ensuring that the overall low frequency gain is exactly 1.

Experimentally, we found that the gain of the filters was < 1 even with $V_{gain-} = 0$. However, the loop as designed could only decrease the gain further by increasing V_{gain-} and the current through M_3 . The most likely reason for the lowered gain is poorly-modeled parasitic resistances and inductances on the ground node, which increase the effective value of R_{s2} . A simple improvement, to be made in future iterations, is to modify the feedback loop so that it can both add and subtract current from M_2 . A simple way to do this is by adding the pMOS transistor M_4 (see Fig. 9). We can now increase the gain by lowering V_{gain+} , which increases the DC current through M_4 , thus causing g_{m2} to increase without affecting g_{m1} .

The bias voltage V_{ref} sets the value of g_{m2} and g_{m1} . The amount of peaking, or quality factor of each stage is approximately $g_{m1} \sqrt{L_1/C_1}$, so we can control the sharpness of the cochlear transfer functions by changing g_{m1} via V_{ref} , which is set by the feedback loop shown in Fig. 10. Consider the amplifier formed by M_2 , which is a replica of the transistor M_2 within the filter stages, and R_L . The loop measures input and output amplitudes and adjusts V_{ref} until this amplifier has a gain of 1 at the oscillator frequency (22 MHz). This gain is approximately $g_{m2,eff} R_L$, where $g_{m2,eff} = g_{m2}/(g_{m2} R_2 + 1)$ and R_2 is designed to be equal to R_{s2} . Thus, the loop sets $g_{m2,eff} = 1/R_L$, and by adjusting R_L with a resistive DAC, we can control the

peak gain, frequency resolution and power consumption of the cochlea. The switch and monostable (one-shot) resets V_{ref} if it exceeds a reference value V_{max} , thus ensuring that the loop does not get stuck at the wrong operating point. This precaution is necessary because the relationship between V_{ref} and gain is not monotonic: for very high values of V_{ref} , the gain drops because the transistor M_2 comes out of saturation.

The envelope detectors were based on diode-connected transistors, and produce pseudo-differential outputs. As in the bidirectional cochlea, their effective dead-zone of ϕ_T/κ was reduced by using pre-amplifiers. The amplifiers, shown in Fig. 11(a), were two-stage, resistively loaded, common-source designs with a total gain of ≈ 16 dB; in the first few filters they were inductively shunt-peaked to increase bandwidth. The bias current was set using a current source at the transistor's source terminal that was bypassed at RF by the capacitor C_{hp} , thus creating a high-pass characteristic. Since the filter outputs themselves are low-pass, the preamplifier outputs are bandpass in nature, which improves their rejection of large, low-frequency signals.

The chip contained a broadband, low-noise amplifier (LNA) at its input (high-frequency end). The LNA, shown in Fig. 11(b), used a common-gate topology with inductive shunt peaking. It had a gain of ≈ 10 dB and was designed to provide a resistive input impedance of $R_{in} = 50 \Omega$. The frequency response of the LNA was high-pass, with a cut-in frequency of $1/(2\pi C_{in} R_{in})$. Chip parameters like R_L and pre-amplifier and LNA bias currents were set by DACs. DAC values were programmed via a three-pin serial interface.

C. Passive Network Synthesis

All circuits were designed in the 8-metal UMC 0.13 μm standard CMOS process. Element values in the passive networks that realize Z'_n and H_n were found by a numerical optimization routine written using Mathematica (Wolfram Research, Champaign, IL). The routine accepts a given network topology as input and finds a set of component values (R, L, C, M)

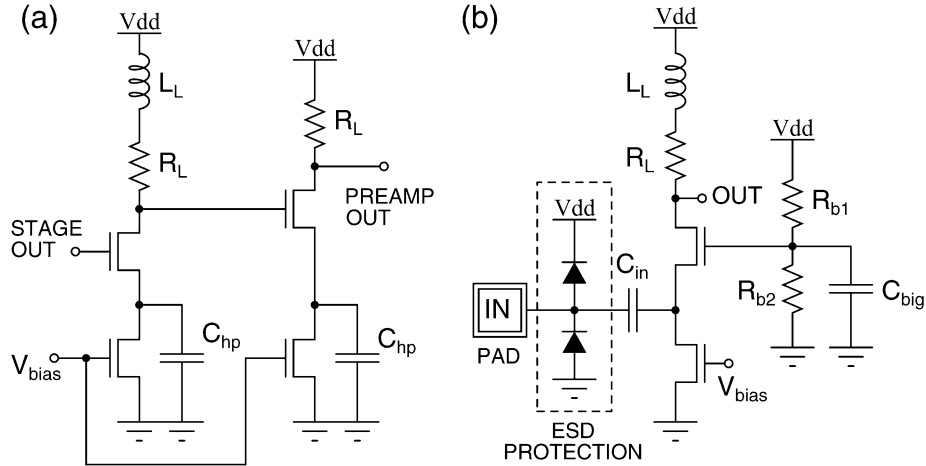


Fig. 11. Circuits used in the unidirectional cochlea chip, (a) the preamplifier within each stage, and (b) the LNA at the input terminal.

that realizes the symbolically-specified, rational driving-point impedance or transfer function. Since network synthesis is, in general, a one-to-many problem, the routine finds one of the infinite set of possible solutions. This set can be restricted by imposing additional conditions on the component values. For example, we restricted the sizes of the two inductors in the transformer to be within 20% of each other. This condition allows similarly-sized coils to be used to realize them, maximizing coupling $k = M/\sqrt{L_1 L_2}$ for a given layout area. The following *impedance and frequency normalized* element values were produced by the routine:

- Z'_n in the bidirectional cochlea: $L_1 = 0.88$ H, $L_2 = 0.61$ H, $M = 0.50$ H, $C_1 = 0.52$ F, $C_2 = 0.60$ F, $C_C = 2.62$ F, $R_1 = -1.3$ Ω and $R_2 = 1.79$ Ω .
- H_n in the unidirectional cochlea: $L_1 = 0.76$ H, $L_2 = 0.60$ H, $M = 0.61$ H, $C_1 = 0.81$ F, $C_2 = 1.47$ F, $C_C = 0.64$ F, $1/g_m = 0.53$ Ω , $R_1 = 0.63$ Ω , $R_2 = 0.11$ Ω .

These normalized values were scaled with Z_0 and $\omega_c(i)$ for implementation. Optimized physical design of the magnetic components (inductors and transformers) was important for realizing the whole system. Details may be found in the Appendix. Capacitors were either of the vertical-field, parallel-plate type or the interleaved horizontal/fringing-field type. In this process the latter has higher capacitance density, which is desirable for minimizing chip area, but also somewhat higher parasitic capacitances to the substrate.

V. MEASUREMENTS

Each cochlea chip was wire-bonded to a printed circuit board for testing. Because of the limited number of pins available, output voltages from the ED present inside every stage were time-multiplexed onto a single bus using a token-passing circuit. The voltages were digitized and captured using a digital oscilloscope and custom software written in LabVIEW (National Instruments, Austin, TX). Further post-processing was performed using MATLAB. At a scan rate of 10 kHz for each channel, we estimate that our measurement noise floor (set by quantization noise from the oscilloscope) is approximately 35 μ V (rms), resulting in a displayed average noise envelope of 100 μ V

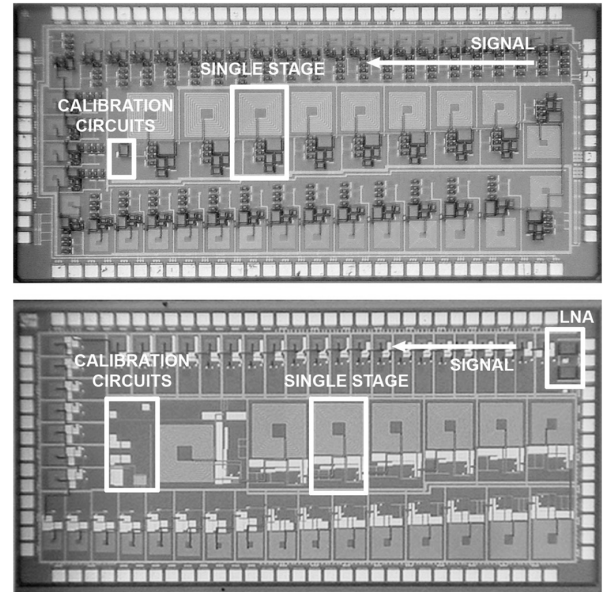


Fig. 12. Bidirectional (top) and unidirectional (bottom) cochlea die photographs. Each chip is 3 mm \times 1.5 mm in size.

(-80 dBV). This value is significantly lower than the measured noise level, which is set by output noise from the circuit.

Fig. 12 shows die photographs of both bidirectional and unidirectional RF cochlea chips. In both cases the line or cascade was arranged such that it spiraled inward from the input terminal to save space, in a manner reminiscent of the biological cochlea. Fig. 13 shows the measured input reflection coefficient, $|S_{11}|$, of both the bidirectional and unidirectional chips. The matching bandwidth, defined as the frequency range over which $|S_{11}| < -8$ dB, was DC to 7.2 GHz for the former and 400 MHz to 3.6 GHz for the latter. The low-frequency limit in the unidirectional case was set by the cut-in frequency of the common-gate LNA. Matching at high frequencies was limited by chip packaging. Packages attenuate high frequency signals because of bond-wire inductances and bond-pad capacitances, which together form low-pass filters.

The bidirectional chip contained $N = 50$ stages with $N_{\text{nat}} = 24$. The values of L_1 and L_2 ranged from 1 nH to 12 nH. Fig. 14

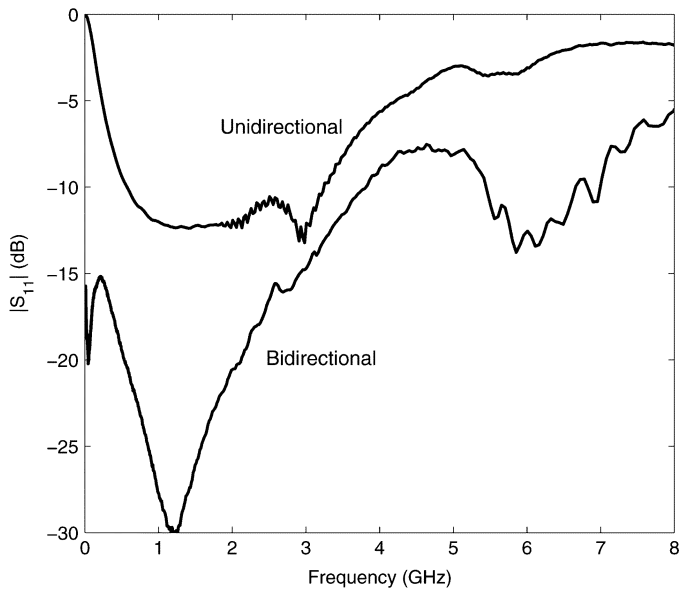


Fig. 13. Measured input reflection coefficients of the bidirectional and unidirectional cochlea chips.

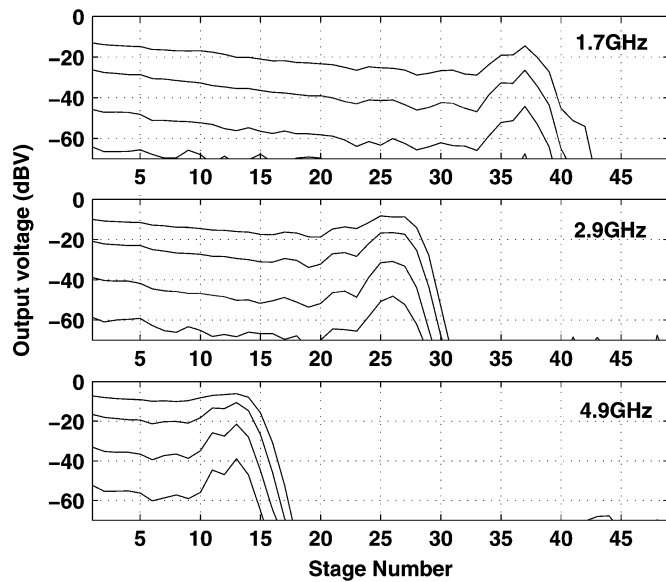


Fig. 14. Bidirectional cochlea spatial responses. Output voltage amplitudes were measured from each stage at the following power levels: -30 , -20 , -10 , and 0 dBm.

shows the measured frequency-to-space transformation of the bidirectional cochlea at different input power levels. The operating frequency range was approximately 1.2 GHz to 8 GHz, with a measured output noise floor of approximately -82 dBV (rms). As expected, the transfer functions resemble asymmetric bandpass filters, with much steeper roll-offs towards the apical, or low-frequency sides of the peaks. However, they show negative slopes in regions significantly basal to the peaks. This behavior is due to two reasons: attenuation due to series line loss, and measurement error due to the dead-zone of the EDs, which causes the RF to DC conversion gain to decrease exponentially for stage outputs smaller than ≈ 5.5 mV_{pp}.

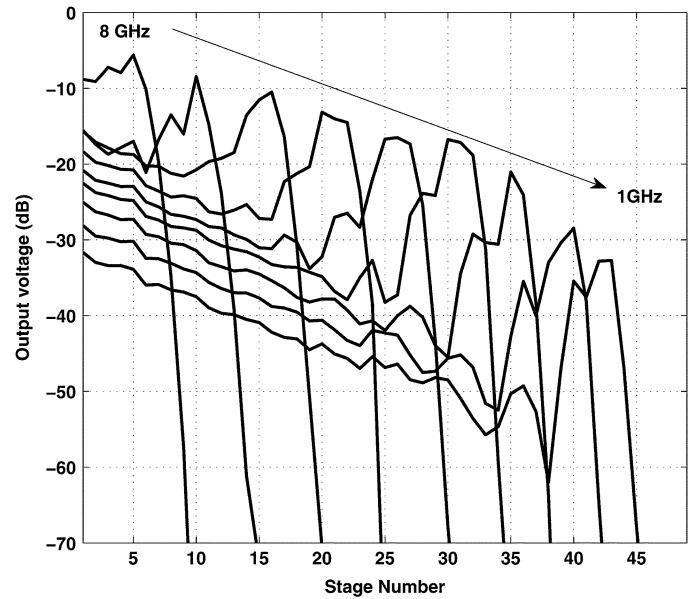


Fig. 15. Spatial responses of the bidirectional RF cochlea to exponentially-spaced input frequencies varying between 1 GHz and 8 GHz. The input power level was fixed at -10 dBm.

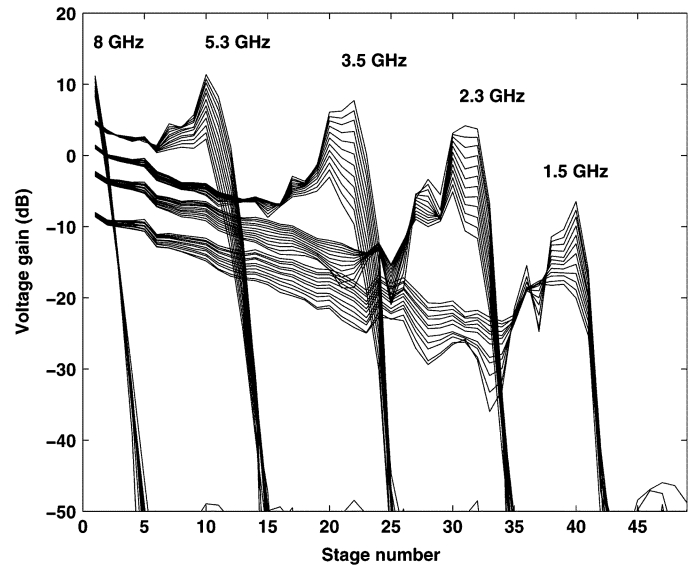


Fig. 16. Spatial responses of the bidirectional RF cochlea at various frequencies obtained while varying the value of the active element within each stage. The bias voltage V_B that sets this negative resistance R_1 was increased from 0.56 V to 0.67 V in 10 mV steps.

Fig. 15 shows measured spatial responses of the bidirectional cochlea to exponentially-spaced input frequencies varying between 1 GHz and 8 GHz, with the input power level fixed at -10 dBm. Fig. 16 shows how the spatial response at various frequencies changes if the value of the negative resistance, R_1 is changed by varying the bias voltage V_B . The peak gain increases as V_B is increased, decreasing the value of R_1 .

Fig. 17 shows spatial responses of the bidirectional cochlea at -10 dB input level for various values of the line loss cancellation resistance R_{LL} . The value of R_{LL} can be varied by changing the bias voltage V_{B2} . We see that a significant amount of line loss can be cancelled by increasing V_{B2} , which

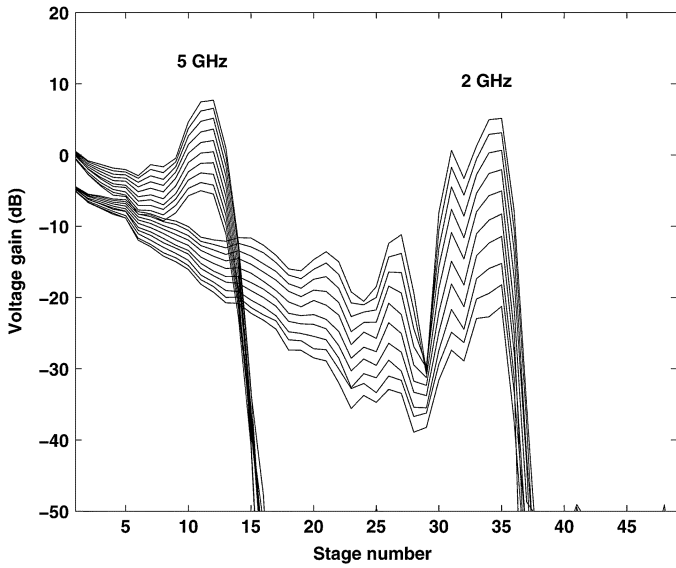


Fig. 17. Spatial responses of the bidirectional RF cochlea at various frequencies obtained while varying the value of the series loss cancellation within each stage. The bias voltage V_{B2} that sets this negative resistance R_{LL} was increased from 0.40 V to 0.58 V in 20 mV steps.

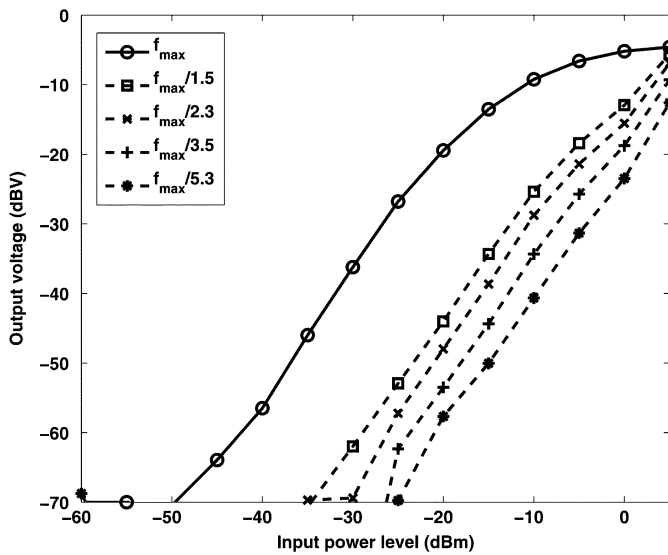


Fig. 18. Measured compression curves of the bidirectional RF cochlea. The spatial location was fixed at the point where maximum response was obtained for $f_{max} = 5.3$ GHz, and the response to frequencies below f_{max} was measured at several power levels.

decreases R_{LL} . However, small values of R_{LL} disturb the local impedance, causing unwanted reflections of the traveling wave that show up as secondary peaks in these spatial responses. This effect limits the amount of cancellation that can be applied.

Fig. 18 shows how the peak gain of the bidirectional cochlea responses decreases with increasing input amplitude. These compression curves were taken by observing the response at a fixed location, the best position for $f_{max} = 5.3$ GHz, to various input frequencies, including f_{max} . We see that the response at f_{max} , being larger, compresses for smaller input power levels than at other frequencies. This behavior is qualitatively similar to that observed in the biological cochlea.

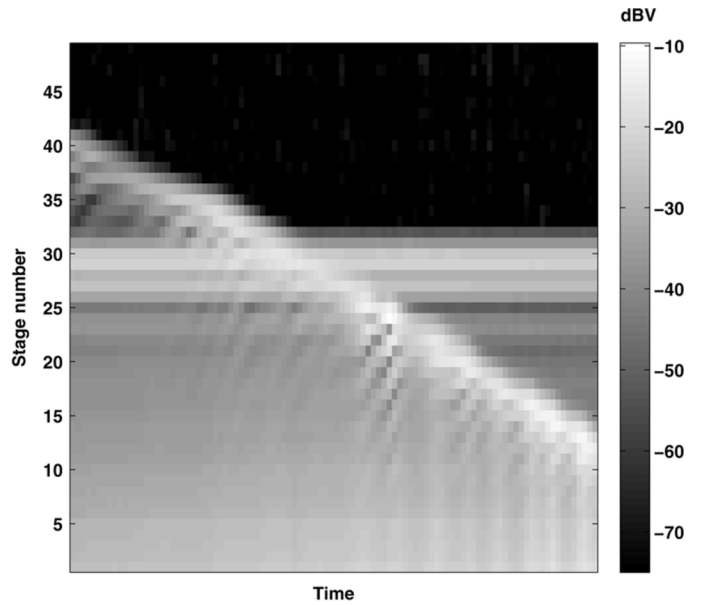


Fig. 19. Measured response of the bidirectional RF cochlea to two simultaneously applied input frequencies. One input was held fixed at 2.4 GHz while the other was increased exponentially from 1 GHz to 8 GHz (left to right in the figure). The power level of both inputs was held fixed at -10 dBm.

Fig. 19 shows a two-tone response: here two input frequencies were simultaneously fed into the bidirectional cochlea. One tone was held fixed at 2.4 GHz, while the other was swept exponentially with time. The cochlear outputs were monitored as a function of time and plotted in the figure. As expected, the spatial response due to the second tone moves linearly with time, while that due to the first remains fixed. Both tones had equal input amplitudes (-10 dBm). Improvements in frequency resolution, especially in the presence of noise, can be obtained by using the phase information, such as temporal correlations between stages, present within cochlear transfer functions [33], [34].

Our unidirectional cochlea chip contained $N = 51$ stages with $N_{nat} = 16$. Spatial responses were broadly similar to those obtained from the bidirectional cochlea, but secondary peaks due to inter-stage reflections were absent because of the unidirectional nature of the cascade. This property allows a lower value of N_{nat} to be used, which reduces noise, power consumption and chip area at the cost of frequency resolution. Our usable frequency range is between 600 MHz and 6 GHz. The peak voltage gain and output noise are both higher for this cochlea, resulting in better input-referred sensitivity (approximately -80 dBm over the “best octave”, 2–4 GHz).

Fig. 20 shows spatial responses of the unidirectional cochlea to three input frequencies and four power levels. The frequency-to-space transform is clearly visible, as is gain compression at high input power levels. The low-frequency gain of each cochlear stage was slightly less than 1 and could not be increased, for reasons described in Section IV.B. As a result, as the input frequency decreased the peak gain of the cochlear transfer function increased, as expected, but then decreased instead of saturating to a constant value. This behavior explains why intermediate input frequencies, such as the 2.4 GHz tone

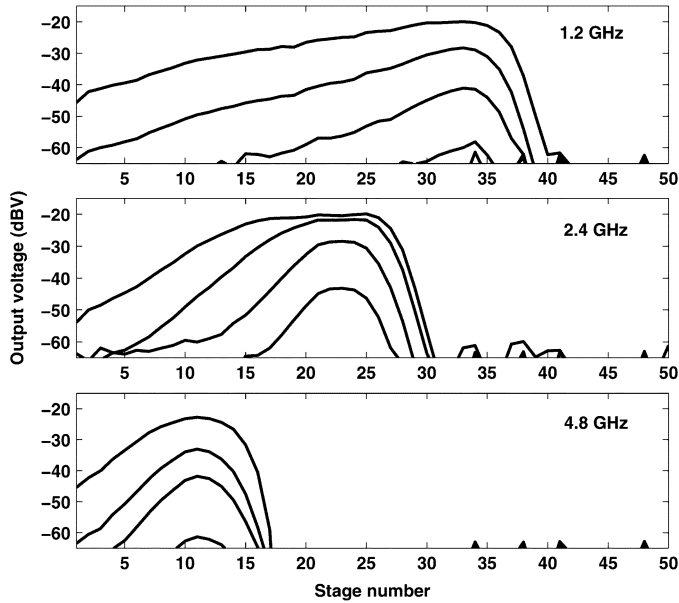


Fig. 20. Spatial responses of the unidirectional cochlea to different input frequencies at the following power levels: -30 , -40 , -50 , -60 dBm.

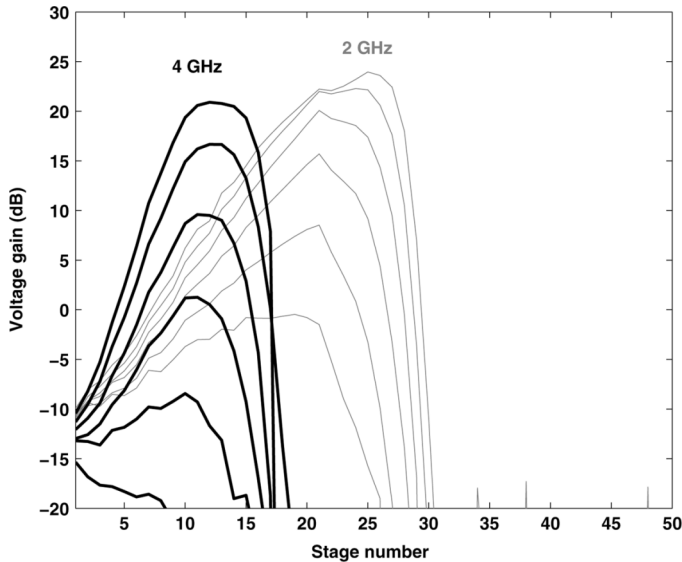


Fig. 21. Spatial responses of the unidirectional cochlea to two different input frequencies for different values of the gain-control resistor R_L .

in Fig. 20, have the highest peak gains and display the most gain compression.

Fig. 21 shows that we can control the peak gain of the cochlear transfer functions by changing the value of R_L , the load resistor shown in Fig. 10. The figure shows spatial responses at 2 and 4 GHz for different values of $R_L = 1\text{k}\Omega/D$, where D is the digital code of the 5-bit DAC that sets R_L . In this case D was increased from 11 to 16, decreasing R_L from $91\ \Omega$ to $67\ \Omega$. The result is increased voltage gain. However, power consumption also goes up, because the transconductance of the transistors M_1 and M_2 inside each filter must increase to keep the gain $g_{m2,\text{eff}}R_L$ fixed at 1. In this case power consumption increased from 200 mW to 300 mW.

TABLE I
PERFORMANCE SUMMARY

Parameter	Bidirectional	Unidirectional
Technology	0.13 μm CMOS	0.13 μm CMOS
Stages per e-fold, N_{nat}	24	16
Total number of stages, N	50	51
Frequency range, GHz	1.2-8	0.6-6
Maximum output noise, $\text{dB}V_{\text{rms}}$	-70	-55
Peak voltage gain, dB	10	35
Maximum output SNR, dB	60	35
Input dynamic range, dB	70	70
Input impedance, Ω	50	50
Typical power consumption	170mA, 1.8V	220mA, 1.3V

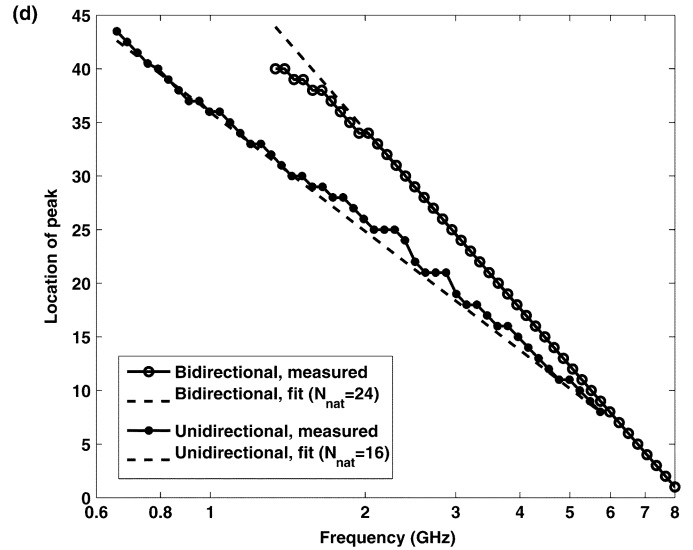


Fig. 22. Measured frequency-to-space transform for the unidirectional and bidirectional cochleas, showing the location of the peak response as a function of input frequency.

The performance of both cochleas is summarized in Table I. In the table, peak voltage gain refers to the gain experienced by small signals (no gain compression). In addition, the quoted dynamic range is for single input tones, with the maximum signal being set by gain compression, and the minimum signal by the input-referred noise floor. The presence of other tones will reduce dynamic range due to two-tone suppression, which is seen in the biological cochlea and also in our cochlea. Two-tone suppression is beneficial in recognizing dominant tones in noisy environments and has led to bio-inspired spectral-analysis algorithms that help improve hearing in noise for the deaf [35], [36].

Fig. 22 summarizes the frequency-to-place transform measured for both designs. Deviations from exponential scaling are visible at the low frequency end of the bidirectional design and are caused by the fact that our simple line-termination network cannot perfectly approximate the line impedance at all frequencies. A higher order termination network can be used to reduce this effect. Deviations from exponential scaling in the unidirectional design were mainly caused by gain compression, which makes it difficult to determine the location of the peak response.

VI. SUMMARY

We have described two real-time, on-chip spectrum analyzers that may be useful for power-and-hardware efficient front ends

in software, cognitive, and ultra-wideband radios. Such radios could use real-time scans of the increasingly crowded RF spectrum to adapt their communication strategies. Our analog RF cochlea chips consume about 100 times less power than that required for direct digitization of the entire bandwidth. By performing initial, high-speed filtering, the chips also decrease the bandwidth and power required for later signal processing, such as the use of more conventional narrowband and heterodyning systems to improve the frequency resolution. Our novel rational unidirectional cochlear model can also enable practical audio-frequency silicon cochleas with low group delay and sharp rolloff slopes. Overall, the RF cochlea illustrates that sensory systems found in nature yield architectures that are useful in man-made signal processors. It also provides insight into why the biological cochlea is efficient.

APPENDIX

This Appendix describes our transformer design flow. Unlike resistors and capacitors, inductors and transformers are not standard integrated circuit components, and no models were available. Normally magnetic components are designed by hand, an initial geometry based on an analytical formula being iteratively refined via electromagnetic simulations. While this approach is sufficient for typical RF designs that use a small number of magnetic components, it rapidly becomes tedious when this number increases. In addition, the mapping from transformer values to geometry is one-to-many, so the final geometry may not be optimized for size or quality factor. We decided to automate the design process as much as possible. We used an analytical formula that predicts the inductance value, L , as a function of geometry [37] and derived the following formula for calculating the DC series resistance $R_{s,DC}$ of a N -turn spiral:

$$R_{s,DC} = \left(\frac{\rho}{wt} \right) NM \tan(\pi/M) d_{avg} \quad (29)$$

where ρ is the resistivity of the metal layer, t its thickness, and w the width of each turn. In addition, each turn is assumed to consist of a regular M -sided polygon, d_{out} and d_{in} are the diameters of the circles that inscribe the outer and inner edges of the spiral, respectively, and $d_{avg} = (d_{out} + d_{in})/2$. The AC resistance can be found by taking the skin effect into account [38]:

$$R_s(\omega) \approx R_{s,DC} \left(\frac{\eta}{1 - e^{-\eta}} \right) \quad (30)$$

where $\eta \equiv t/\delta$, and δ is the skin depth. We assumed that ω_c , the center frequency of the stage, was much lower than the self-resonant frequency of the coil. Thus, we were able to analytically find the quality factor $Q_c = \omega_c L/R_s$ of the inductor at ω_c . We then wrote a numerical optimization routine using Mathematica to find the optimal coil geometry. The routine finds the geometry that produces the required value of L while minimizing layout area and also ensuring that Q_c is higher than Q_{min} , a constant. Square coils ($M = 4$) were used because they have the largest inductance for a given layout area. The two coils that form a transformer were laid out on different metal layers; their centers were offset from each other. The amount of offset was varied to control the value of the coupling factor k . This process was repeated for every stage.

An electromagnetic simulator was used to create broadband frequency-domain models, i.e., two-port S-parameters, for each transformer [39]. Next, a model-order reduction routine available in our CAD software (SpectreRF, Cadence Design Systems, San Jose, CA) was used to create lumped equivalent circuit models, suitable for time-domain simulations, from the frequency-domain models. Finally, we wrote a MATLAB (The MathWorks, Natick, MA) program to automatically generate on-chip layouts for these optimal transformer geometries.

ACKNOWLEDGMENT

The authors would like to thank the anonymous reviewers for several valuable suggestions.

REFERENCES

- [1] R. Sarpeshkar, R. F. Lyon, and C. A. Mead, "A low-power wide-dynamic-range analog VLSI cochlea," *Analog Integr. Circuits Signal Process.*, vol. 16, no. 3, pp. 245–274, Aug. 1998.
- [2] J. O. Pickles, *An Introduction to the Physiology of Hearing*, 2nd ed. London, U.K.: Academic Press, 1988.
- [3] C. D. Geisler, *From Sound to Synapse: Physiology of the Mammalian Ear*, 1st ed. Oxford, U.K.: Oxford Univ. Press, 1998.
- [4] W. E. Brownell, C. R. Bader, D. Bertrand, and Y. de Ribaupierre, "Evoked mechanical responses of isolated cochlear outer hair cells," *Science*, vol. 259, pp. 194–196, Jan. 1985.
- [5] P. Dallos, B. N. Evans, and R. Hallworth, "Nature of the motor element in electrokinetic shape changes of cochlear outer hair cells," *Nature*, vol. 350, pp. 155–157, Mar. 1991.
- [6] P. Dallos and B. N. Evans, "High-frequency motility of outer hair cells and the cochlear amplifier," *Science*, vol. 267, no. 5206, pp. 2006–2009, Mar. 1995.
- [7] G. Frank, W. Hemmert, and A. W. Gummer, "Limiting dynamics of high-frequency electromechanical transduction of outer hair cells," *Proc. Natl. Acad. Sci. USA*, vol. 96, pp. 4420–4425, Apr. 1999.
- [8] J. Ludwig, D. Oliver, G. Frank, N. Klöcker, A. W. Gummer, and B. Fakler, "Reciprocal electromechanical properties of rat prestin: The motor molecule from rat outer hair cells," *Proc. Natl. Acad. Sci. USA*, vol. 98, no. 7, pp. 4178–4183, Mar. 2001.
- [9] L. Robles and M. A. Ruggero, "Mechanics of the mammalian cochlea," *Physiol. Rev.*, vol. 81, no. 3, pp. 1305–1352, Jul. 2001.
- [10] C. A. Shera, "Intensity-invariance of fine time structure in basilar-membrane click responses: Implications for cochlear mechanics," *J. Acoust. Soc. Am.*, vol. 110, no. 1, pp. 332–348, Jul. 2001.
- [11] C. A. Shera, "Mammalian spontaneous otoacoustic emissions are amplitude-stabilized cochlear standing waves," *J. Acoust. Soc. Am.*, vol. 114, no. 1, pp. 244–262, Jul. 2003.
- [12] T. K. Lu, S. Zhak, P. Dallos, and R. Sarpeshkar, "Fast cochlear amplification with slow outer hair cells," *Hearing Research*, vol. 214, no. 1–2, pp. 45–67, Apr. 2006.
- [13] A. Hajimiri, "Distributed integrated circuits: An alternative approach to high-frequency design," *IEEE Commun. Mag.*, vol. 40, no. 2, pp. 168–173, Feb. 2002.
- [14] E. Afshari, H. S. Bhat, A. Hajimiri, and J. E. Marsden, "Extremely wideband signal shaping using one- and two-dimensional nonuniform nonlinear transmission lines," *J. Appl. Phys.*, vol. 99, no. 5, p. 054901, Mar. 2006.
- [15] D. S. Ricketts, X. Li, N. Sun, K. Woo, and D. Ham, "On the self-generation of electrical soliton pulses," *IEEE J. Solid-State Circuits*, vol. 42, no. 8, pp. 1657–1668, Aug. 2007.
- [16] E. Afshari, H. S. Bhat, and A. Hajimiri, "Ultrafast analog Fourier transform using 2-D LC lattice," *IEEE Trans. Circuits Syst. I*, vol. 55, no. 8, pp. 2332–2343, Aug. 2008.
- [17] G. E. R. Cowan, R. C. Melville, and Y. P. Tsvividis, "A VLSI analog computer/digital computer accelerator," *IEEE J. Solid-State Circuits*, vol. 41, no. 1, pp. 42–53, Jan. 2006.
- [18] R. F. Lyon and C. A. Mead, "An analog electronic cochlea," *IEEE Trans. Acoust. Speech Signal Process.*, vol. 36, no. 7, pp. 1119–1134, Jul. 1988.
- [19] A. G. Andreou, "Electronic arts imitate life," *Nature*, vol. 354, pp. 501–501, Dec. 1991.

- [20] W. Liu, A. G. Andreou, and M. H. Goldstein, Jr., "Voiced-speech representation by an analog silicon model of the auditory periphery," *IEEE Trans. Neural Networks*, vol. 3, no. 3, pp. 477–487, May 1992.
- [21] L. Watts, D. A. Kerns, R. F. Lyon, and C. A. Mead, "Improved implementation of the silicon cochlea," *IEEE J. Solid-State Circuits*, vol. 27, no. 5, pp. 692–700, May 1992.
- [22] T. Hinck, Z. Yang, Q. Zhang, and A. Hubbard, "A current-mode implementation of a traveling wave amplifier model similar to the cochlea," in *Proc. IEEE Int. Symp. Circuits and Systems (ISCAS'99)*, 1999, vol. 2, pp. 228–231.
- [23] S. Zhak, S. Mandal, and R. Sarpeshkar, "A proposal for an RF cochlea," in *Proc. Asia Pacific Microwave Conf.*, Dec. 2004.
- [24] S. Mandal, S. Zhak, and R. Sarpeshkar, "Circuits for an RF cochlea," in *Proc. IEEE Int. Symp. Circuits Syst. (ISCAS 2006)*, May 2006, pp. 2845–2848.
- [25] C. Galbraith, R. D. White, K. Grosh, and G. M. Rebeiz, "A mammalian cochlea-based RF channelizing filter," in *IEEE MTT-S Int. Microwave Symp. Dig.*, 2005, p. 4.
- [26] C. Galbraith, G. Rebeiz, and R. Drangmeister, "A cochlea-based pre-selector for UWB applications," in *IEEE Radio Frequency Integrated Circuits (RFIC) Symp.*, 2007, pp. 219–222.
- [27] C. Galbraith, R. D. White, L. Cheng, K. Grosh, and G. M. Rebeiz, "Cochlea-based RF channelizing filters," *IEEE Trans. Circuits Syst. I*, vol. 55, pp. 969–979, 2008.
- [28] G. Zweig, "Finding the impedance of the organ of corti," *J. Acoust. Soc. Am.*, vol. 89, no. 3, pp. 1229–1254, Mar. 1991.
- [29] E. M. Williams, "Radio-frequency spectrum analyzers," *Proc. Inst. Radio Eng.*, vol. 34, no. 1, pp. 18–22, Jan. 1946.
- [30] S. M. Zhak, "Modeling and design of an active silicon cochlea," Ph.D. dissertation, Massachusetts Inst. Technol., Cambridge, MA, Sep. 2008.
- [31] L. Watts, "Cochlear mechanics: analysis and analog VLSI," Ph.D. dissertation, California Inst. Technol., Computation and Neural Systems, Pasadena, CA, Apr. 1993.
- [32] S. Puria and J. Allen, "A parametric study of cochlear input impedance," *J. Acoust. Soc. Am.*, vol. 89, no. 1, pp. 287–309, Jan. 1991.
- [33] X. Yang, K. Wang, and S. A. Shamma, "Auditory representations of speech signals," *IEEE Trans. Inf. Theory*, vol. 38, no. 2, pp. 824–839, Mar. 1992.
- [34] J. W. Wang, R. Sarpeshkar, M. Jabri, and C. Mead, "A low power analog front end module for cochlear implants," in *Proc. XVI World Congr. Otorhinolaryngology, Head and Neck Surgery*, Sydney, Australia, Mar. 1997.
- [35] L. Turicchia and R. Sarpeshkar, "A bio-inspired companding strategy for spectral enhancement," *IEEE Trans. Speech Audio Process.*, vol. 13, no. 2, pp. 243–253, Mar. 2005.
- [36] A. Bhattacharya and F. G. Zeng, "Companding to improve cochlear-implant speech recognition in speech-shaped noise," *J. Acoust. Soc. Am.*, vol. 122, no. 2, pp. 1079–1089, Aug. 2007.
- [37] S. S. Mohan, M. del Mar Hershenson, S. P. Boyd, and T. H. Lee, "Simple accurate expressions for planar spiral inductances," *IEEE J. Solid-State Circuits*, vol. 34, no. 10, pp. 1419–1424, Oct. 1999.
- [38] T. H. Lee, *The Design of CMOS Radio-Frequency Integrated Circuits*, 2nd ed. Cambridge, U.K.: Cambridge Univ. Press, 2004.
- [39] A. M. Niknejad, ASITIC: Analysis and Simulation of Spiral Inductors and Transformers for ICs. [Online]. Available: <http://rfic.eecs.berkeley.edu/~niknejad/asitic.html>



Soumyajit Mandal (S'01) received the B.Tech. degree from the Indian Institute of Technology, Kharagpur, India, in 2002, and the S.M. degree in electrical engineering from the Massachusetts Institute of Technology (MIT), Cambridge, MA, in 2004. He is currently working toward the Ph.D. degree at MIT. His research interests include analog and biological computation, nonlinear dynamics, low-power analog and RF circuit design and antennas.

Mr. Mandal was awarded the President of India Gold Medal in 2002.



Serhii M. Zhak received the S.M. degree in physics from the Moscow Institute of Physics and Technology, Russia, in 1999, and the Ph.D. degree in electrical engineering and computer science from Massachusetts Institute of Technology (MIT), Cambridge, MA, in 2008. His research interests include biomedical implants for the deaf, low-power and low-noise integrated analog design, digital and analog feedback and optimal control, power electronics, and integrated radio-frequency circuits. Dr. Zhak is currently with the power management

group at Maxim Integrated Products.



Rahul Sarpeshkar (M'97) received the S.B. degree in electrical engineering and the S.B. degree in physics from the Massachusetts Institute of Technology (MIT), Cambridge, MA, in 1990 and the Ph.D. degree from the California Institute of Technology, Pasadena, in 1997.

He was with Bell Labs as a Member of the Technical Staff in 1997. Since 1999 he has been on the faculty of the Electrical Engineering and Computer Science Department at MIT, where he heads a research group on Analog VLSI and Biological Systems and

is currently an Associate Professor. He holds over 20 patents and has authored more than 90 publications, including one that was featured on the cover of *Nature*. His website is <http://www.rle.mit.edu/avbs>.

Dr. Sarpeshkar has received the Packard Fellow Award given to outstanding young faculty, the Office of Naval Research Young Investigator Award, the National Science Foundation Career Award, and the Indus Technovator Award. He has also received the Junior Bose Award and the Ruth and Joel Spira Award, both for excellence in teaching at MIT. He is currently an Associate Editor of *IEEE TRANSACTIONS ON BIOMEDICAL CIRCUITS AND SYSTEMS*. His research interests include analog and mixed-signal VLSI, biomedical systems, ultra low power circuits and systems, biologically inspired circuits and systems, molecular biology, neuroscience, and control theory.